

M. Lehen, A. Alonso, G. Arnoux, N. Baumgarten, S.A. Bozhenkov, S. Brezinsek,
M. Brix, T. Eich, S.N. Gerasimov, A. Huber, S. Jachmich, U. Kruezi, P.D. Morgan,
V.V. Plyusnin, C. Reux, V. Riccardo, G. Sergienko, M.F. Stamp
and JET EFDA contributors

Disruption Mitigation by Massive Gas Injection in JET

Disruption Mitigation by Massive Gas Injection in JET

M. Lehnen¹, A. Alonso², G. Arnoux³, N. Baumgarten¹, S.A. Bozhenkov⁴, S. Brezinsek¹,
M. Brix³, T. Eich⁴, S.N. Gerasimov³, A. Huber¹, S. Jachmich⁵, U. Kruezi¹, P.D. Morgan³,
V.V. Plyusnin⁶, C. Reux⁷, V. Riccardo³, G. Sergienko¹, M.F. Stamp³
and JET EFDA contributors*

JET-EFDA, Culham Science Centre, OX14 3DB, Abingdon, UK

¹*Institute for Energy Research - Plasma Physics, Forschungszentrum Jülich, Association
EURATOM-FZJ, Trilateral Euregio Cluster, 52425 Jülich, Germany*

²*Laboratorio Nacional de Fusion, Asociacion EURATOM-CIEMAT, Madrid, Spain*

³*EURATOM-CCFE Fusion Association, Culham Science Centre, OX14 3DB, Abingdon, OXON, UK*

⁴*Max-Planck-Institut für Plasmaphysik, EURATOM-Assoziation, D-85748 Garching, Germany*

⁵*Laboratoire de Physique des Plasmas-Laboratorium voor Plasmafysica, Association
EURATOM-Belgian State, ERM/KMS, B-1000 Brussels, Belgium*

⁶*Instituto de Plasmas e Fusão Nuclear/IST, Associacao EURATOM-IST, Av. Rovisco Pais, 1049-001 Lisbon, Portugal*

⁷*CEA, IRFM, F-13108 Saint-Paul-lez-Durance, France*

* See annex of F. Romanelli et al, "Overview of JET Results",
(23rd IAEA Fusion Energy Conference, Daejeon, Republic of Korea (2010)).

“This document is intended for publication in the open literature. It is made available on the understanding that it may not be further circulated and extracts or references may not be published prior to publication of the original when applicable, or without the consent of the Publications Officer, EFDA, Culham Science Centre, Abingdon, Oxon, OX14 3DB, UK.”

“Enquiries about Copyright and reproduction should be addressed to the Publications Officer, EFDA, Culham Science Centre, Abingdon, Oxon, OX14 3DB, UK.”

The contents of this preprint and all other JET EFDA Preprints and Conference Papers are available to view online free at www.iop.org/Jet. This site has full search facilities and e-mail alert options. The diagrams contained within the PDFs on this site are hyperlinked from the year 1996 onwards.

ABSTRACT.

Disruption mitigation is mandatory for ITER in order to reduce forces and to mitigate heat loads during the Thermal Quench (TQ) and from runaway electrons. A fast Disruption Mitigation Valve (DMV) has been installed at JET to study mitigation by Massive Gas Injection (MGI). Different gas species and amounts have been investigated with respect to timescales and mitigation efficiency. We discuss the mitigation of halo currents as well as sideways forces during vertical displacement events, the mitigation of heat loads by increased energy dissipation through radiation, the heat loads which could arise by asymmetric radiation and the suppression of runaway electrons.

1. INTRODUCTION

The mitigation of thermal and mechanical loads during disruptions is an urgent task to be solved for ITER to ensure the integrity of Plasma-Facing Components (PFC). However, extreme loads are already an issue for present day machines like JET, with its new ITERlike wall, having the material used in ITER for DT operation [1]. Reduction of such loads to tolerable values is needed, consequently the generation of high-energy electrons (so-called Runaway Electrons - RE) is of special concern. RE in JET can carry currents of up to 50% of plasma current before the disruption, leading to a fast and localised deposition of several MJ on main chamber PFC [2, 3]. The experiments reported here were performed in a full graphite environment in preparation of a potential mitigation system for the JET ITER-like wall.

Disruption mitigation has to fulfill three aims: mitigation of forces from halo and eddy currents, mitigation of convective/conductive heat loads during the thermal quench, mitigation of heat loads from runaway electrons. ITER needs a reduction of the expected forces by a factor 2 – 3 and a reduction of the thermal loads on Be and W components by at least a factor 10 to ensure integrity and lifetime of PFC [4]. Beside the efforts taken for disruption avoidance, two main mitigation techniques have been followed up so far as last resort in the case of an unavoidable disruption: massive gas injection and pellet injection. The latter was for some time regarded as not feasible because of low assimilation of material in the plasma. However, new concepts are developed to overcome this drawback [5]. Massive gas injection is presently the most explored technique and is studied at many tokamaks: Alcator C-mod [6], ASDEX Upgrade [7], DIII-D [8], JT60-U [9], MAST [10], TEXTOR [11] and Tore Supra [12].

A fast valve (Disruption Mitigation Valve - DMV) has been installed at JET to study disruption mitigation by massive gas injection [13, 14, 15, 16]. The valve is positioned on top of the machine and the gas is guided by a 4m long tube to the plasma. Gas species investigated are helium, neon, argon and mixtures of these with 90% of deuterium as well as pure deuterium. With a volume of the injection chamber of $0.65 \times 10^{-3} \text{ m}^3$, a maximum pressure of 3.6MPa and a total release of about 50% of the stored gas, up to 2.5×10^{23} particles can be injected, corresponding to about 100 times the electron content in the plasma.

The target plasmas studied here have low shaping with triangularity $\delta = 0.24\text{--}0.29$ and elongation $\kappa = 1.7$, the equilibrium reconstruction is given in figure 1. We studied mainly MGI into ohmic

plasmas and neutral beam heated H-mode plasmas with up to $P_{\text{NBI}} = 18\text{MW}$. The plasma current varied between $I_p = 1.5\text{MA}$ to 2.5MA , but was set for most studies to $I_p = 2.0\text{MA}$. The toroidal magnetic field varied between $B_T = 1.8\text{T}$ and 3.0T . Typical density and temperature profiles as measured with high resolution Thomson scattering are given in figure 2.

Figure 3 shows the sequence of a typical JET disruption triggered by injection of about 2×10^{23} particles of the Ar/D₂ mixture into a NBI heated plasma. After the activation of the DMV, the gas flows through the tube and arrives after a delay of about 2ms at the plasma edge. At that time the cooling of the plasma edge starts and part of the thermal energy is dissipated by line radiation. Eventually, the thermal quench is triggered when the cooling front arrives at the critical flux surface and the remaining thermal energy is released within 1.5 ms as indicated by Soft X-Ray radiation (SXR). The thermal quench is followed by the decay of the plasma current caused by the high resistivity of the remaining low temperature plasma.

2. PRE-THERMAL-QUENCH PHASE

The pre-thermal-quench phase includes the Time-Of-Flight (TOF) of the gas from the valve to the plasma edge and the duration of the edge cooling process prior to the initiation of the Thermal Quench (TQ). The TOF depends on the sound speed C_0 of the injected species and thus mainly on the mass. From the theory of non-stationary adiabatic expansion into vacuum, the gas front arrives at the plasma edge after a time $\Delta t = L/3c_0$, where $L = 4.5\text{ m}$ and $c_0 = \sqrt{\gamma RT/M}$, with the adiabatic index γ being $7/5$ for molecules and $5/3$ for atoms. This theoretical TOF is compared in figure 4 with the experimental one found from different diagnostics. The outermost channel of the Electron Cyclotron Emission (ECE) radiometer has been used to detect the first drop in temperature (see also [13]), the bolometry channel indicated in figure 1 has been used to detect the increase in radiation and the interferometer has been used to detect the first rise in electron density. All three diagnostics are toroidally 45° away from the position of the DMV. The time resolution of ECE and bolometry is $200\mu\text{s}$, the time resolution of the interferometer is $10\mu\text{s}$. The injected species are D₂ ($M = 4$), $90\%D_2 + 10\%Ne$ ($M = 5.6$), $90\%D_2 + 10\%Ar$ ($M = 7.6$), Ne ($M = 20$) and Ar ($M = 40$). Although there is some systematic difference in the TOF found from these diagnostics, they all agree reasonably well with the theoretical prediction and we will use the theoretical TOF in the following analysis.

Figure 5a shows the cooling duration for various species and pressure. This time is defined as the delay between DMV activation and the start of the Current Quench (CQ) as indicated by the positive peak in the plasma current and includes therefore also the duration of the thermal quench. The TOF has been subtracted. The cooling duration decreases not only with the number of injected particles, but also with the safety factor q_{95} , indicating that the thermal quench is initiated when the cooling front reaches a critical flux surface (presumably $q = 2$). Pure neon and argon as well as the mixtures with deuterium have a much shorter cooling duration compared to pure deuterium and helium. Due to technical reasons, helium injection was done only with helium plasma. However, injection of other species into helium plasma show that the timescales are determined by the injected species and not by the plasma species.

Beside the importance for the overall reaction time of the MGI system, the duration of the cooling phase has impact on the efficiency of the gas injection. The greater the quantity of injected gas, the shorter the pre-TQ phase and, therefore, less time is available for the gas injection. The assimilation of gas injected after the thermal quench is assumed to be much less efficient and is not contributing to the mitigation of heat loads during the TQ. Figure 5b gives the number of particles injected before start of the current quench $N_{inj,CQ}$ as calculated from adiabatic expansion into vacuum. This approach has been validated with lab measurements using the JET set-up [17, 18, 19].

The fraction of gas injected before the current quench $f_{inj,CQ}$ decreases with increasing pressure, because of the shorter cooling phase. However, an increase in the absolute number of particles is still achieved.

Obviously, it would be expected that the cooling duration increases with increasing stored energy. This is not generally the case as shown in figure 6. For injection of D_2 mixtures at low pressure, the cooling duration indeed increases with W_{th} . This is also the case, but less pronounced, for the pure gases. But for high pressure injection we find no dependence on the energy for all species. In order to analyse the cooling process in more detail, figure 7 shows the temporal evolution of the plasma current and the radiated power during Ar/ D_2 injection into L- and H-mode discharges, for the minimum and maximum pressure in the DMV. Although the waveform of the gas injection is identical for all four disruptions and, thus, is the amount of injected impurities, the radiated power P_{rad} is in the first phase of the cooling process more than one order of magnitude lower for the L-mode disruptions. This could be partly attributed to the low initial electron density, which is about 3 times higher in the H-mode cases. In this first phase, P_{rad} increases only linearly with the injected amount of gas as indicated by the dashed lines in 7b, which represent the fraction of injected gas P_{rad} times a factor to fit the measured P_{rad} . In the H-mode disruptions, P_{rad} increases proportional to the valve pressure by a factor 7, in L-mode the increase is about a factor 4. In the later phase of the cooling process a strongly non-linear increase of P_{rad} is observed about 1 – 2 ms before the current spike. The large difference in P_{rad} results in a comparable cooling duration for L- and H-mode with strong MGI ($p_{DMV} = 3.5\text{MPa}$), despite the significant difference in thermal energy: $E_{th} \approx 4.5\text{MJ}$ (H-mode)/1.0MJ (L-mode).

The penetration of the cooling front is illustrated in figure 7c, which shows an example of the development of the SXR emission during Ar/ D_2 injection. The signal rises strongly during injection, which is typical especially for the injection of Argon, as the Bremsstrahlung increases significantly. As the cooling front penetrates into the plasma, a successive decay of SXR at the different measuring positions is observed (see figure 1 for the position of the SXR channels). Eventually, the cooling front reaches the critical surface and the thermal quench sets in.

The cooling duration Δt_{pre-TQ} can be estimated from the simple assumption that the thermal quench is initiated after a certain energy W_{pre-TQ} stored outside the critical surface has been dissipated by radiation:

$$W_{req-TQ} = \int_0^{\Delta t_{pre-TQ}} P_{rad} \sim \int_0^{\Delta t_{pre-TQ}} N_Z^\alpha, \quad (1)$$

with $N_Z \sim p_{DMV} f_{inj}$ being the number of injected particles. The exponent α is expected from the observations discussed above to be 1. In order to see, if the cooling duration shows a universal dependence for all injected species, we scaled Δt_{pre-TQ} as shown in figure 5a by a factor for each species such that the data points overlap. These times are quantitatively compared to Δt_{pre-TQ} from equation 1 in figure 8. The scaling of the cooling time of atomic species agrees well with the simple assumption, whereas for molecules (including mixtures with D₂) the dependency is overestimated. However, one has to keep in mind, that the definition for Δt_{pre-TQ} , chosen for practical reasons, includes also most part of the thermal quench, where the radiated power increases very quickly in time.

3. MITIGATION OF FORCES

Massive gas injection aims at a fast current decay in order to mitigate forces from halo currents. Figure 9 shows the linear current decay time extrapolated from the drop in current from 100% to 70% of the pre-TQ current and normalised to the plasma cross section. This definition has been chosen in order to avoid any influence from runaway current plateaux. In [20] it has been shown that the extrapolation range can have strong impact on the estimated decay time. Therefore, we compare in figure 9b with non-MGI references for both definitions, the commonly used 80% to 20% decay and our definition. MGI causes a faster current decay in comparison to most reference disruptions. From the tendency of the standard definition to result in shorter τ_{CQ} it becomes obvious that the CQ in many 'natural' disruptions starts with a slow current decay (most likely because of a weak impurity influx), which accelerates in the later phase of the CQ. With MGI, the current decay is fast from the very beginning of the CQ, which is essential for the mitigation of Vertical Displacement Events (VDE). In order to keep forces from eddy currents tolerable, the current decay time has to stay above the lower bound of $\tau_{CQ}/S = 1.7\text{ms}/\text{m}^2$ for ITER [21]. This limit was reached with pure Ar MGI in JET, however, the definition of τ_{CQ} chosen here can lead to lower values compared to those from the 80% to 20% decay. For D₂ mixtures, where runaway generation is avoided, the difference between the two definitions amounts to about 20%. A saturation of τ_{CQ}/S at larger numbers of injected particles is not obvious from the present database.

Halo currents can generate strong forces on the vessel and on inner wall structures. Especially, the product of halo current fraction I_{halo}/I_p and toroidal peaking factor TPF has to be limited to ensure the integrity of ITER wall components [22]. These halo currents are reduced by MGI, if the thermal quench is initiated before the vertical position has moved significantly in a VDE. Figure 10 shows time traces of deliberate VDEs, which were initiated by a vertical upward kick and a simultaneous switch-off of the vertical stabilisation. The red curves show data from a pure VDE without gas injection, the blue curves show data from a VDE during which the DMV was activated and injected Ar/D₂ with initial pressure of 3.2 MPa. The thermal quench was initiated at the same time for both cases, but the current quench was significantly accelerated with MGI. As a result the halo current was reduced by about a factor 2. Essential for a successful mitigation of halo currents is a fast reaction time. This time depends on the time of flight in the delivery tube and the duration

of the cooling phase until thermal quench as described in section 2. Figure 11 shows the halo current fraction multiplied by the toroidal peaking factor as function of the delay between thermal quench and a vertical displacement of 10cm for a fast VDE ($\tau_{\text{growth}} \approx 5\text{ms}$). The minimum reaction time of 7ms, achieved with the Ar/D₂ mixture, allows a reduction of the halo currents by about 50%, assuming that a vertical displacement of 10 cm is taken as trigger for MGI and that control systems cause no further delay. Beside halo currents, sideways forces caused by toroidal asymmetries in the vertical current moment $\delta M_z = \delta(I_p z_p)$ during the current quench are of concern for ITER [23, 24]. The normalised sideways impulse $\int_{\text{CQ}} \delta M_z dt / 2I_{\text{paP}}$ (integrated over the current quench) is reduced by more than an order of magnitude (figure 11).

4. MITIGATION OF HEAT LOADS

4.1. HEAT LOADS BY CONDUCTION/CONVECTION

Heat loads during the thermal quench can be reduced by enhancing the radiation with extrinsic impurities supplied by MGI. This is in contrast to many non-MGI disruptions, where the impurities are released not until the thermal quench and can therefore radiate only a minor fraction of the thermal energy. In order to quantify the fraction of radiated energy during the different phases of an MGI disruption, one has to carefully define the time windows of these phases. Another restriction arises from the time resolution of the bolometry, which can cause uncertainty during phases of fast rise in the radiated power as it happens in the thermal quench. In the following, we will analyse different approaches to quantify the fraction of radiated energy.

In order to avoid any uncertainties arising from the separation of the different disruption phases, an energy balance can be done by comparing the radiated energy during the whole disruption with the thermal and magnetic energy stored in the plasma before the disruption. The radiated energy is

$$W_{\text{rad}} = f_{\text{rad}} \times (W_{\text{rad}}^{\text{structure}} - W_{\text{rad}} - W_{\text{mag}}^{\text{RE}}) + f_{\text{th}} \times W_{\text{th}}, \quad (2)$$

with $f_{\text{mag}} \approx 1$; it was shown for JET that almost 100% of the ohmic power during the current quench is dissipated by radiation [25]. We analyse only disruptions without generation of runaways ($W_{\text{mag}}^{\text{RE}} = 0$). In figure 12 the radiated energy is shown as function of the thermal energy. The plasma current is 2MA, the magnetic energy $W_{\text{mag}} = 10.8 \pm 0.3\text{MJ}$, accordingly. With the assumption that the dissipation of magnetic energy in the structure $W_{\text{mag}}^{\text{structure}}$ is constant for these disruptions, we find that about 50% of the stored thermal energy is dissipated by radiation with Ar/D₂ and Ne/D₂. For pure D₂ this fraction is only about 10%. For comparison, natural disruptions from a broader JET database with the same magnetic energy are shown as well as a $q = 2$ disruption, caused by deliberate ramp-down of the toroidal magnetic field. The reference disruptions without gas injection show no dependence on W_{th} and a higher $W_{\text{mag}}^{\text{structure}}$ as seen from the extrapolated offset in W_{rad} at $W_{\text{th}} = 0$. Additionally, two data points from VDEs are shown. They indicate a W_{th} of about 30%, which could be the result from the impurity release taking place before the thermal quench, when the plasma touches the upper dump plate [26].

Previously, we defined the start of the current quench to be at the maximum current during the current spike. The end of the thermal quench was defined to be the start of the current quench. This is a practical definition, a more smooth transition from thermal quench to current quench is to be expected. The start of the thermal quench can be defined as the start of the decay in SXR. This is more reliable compared to the temperature drop measured by ECE, which is in many MGI disruptions already quite early in cut-off. With this definition of the start and end of the thermal quench, we find from figure 3 for the Ar/D₂ injection into H-mode that up to 50% of the thermal energy is lost predominantly by radiation before the TQ. About 40% of the remaining energy is radiated during the TQ. Thus, 30% of the initial energy would be lost by convection during the TQ. By divertor thermography, we find that typically only about 5% of W_{th} is found in the (outer) divertor [3].

Another and more precise definition for the end of the thermal quench can be used by taking the time where SXR emission is reduced to noise level. With this definition we see from figure 3 that more than 90% of W_{th} are radiated. Figure 13 shows the radiated energy until the end of the thermal quench using this new definition for the same data as presented in figure 12. For the deuterium mixtures we find now that about 90-100% of W_{th} is radiated. This fraction is independent from the pressure in the DMV, showing that already the maximum possible fraction of radiated energy is reached. Pure deuterium radiates only about 40% of W_{th} and VDEs are also in the same range. Injecting gas into a VDE raises the fraction to about 70-80%.

The uncertainty that arise from the latter technique is that during the thermal quench already part of the magnetic energy could be dissipated by radiation as the plasma starts to cool down. This might also explain, that values above 100% are found for low W_{th} . The method to integrate over the whole disruption implies the uncertainty that $W_{mag}^{structure}$ might not be a constant.

4.2. HEAT LOADS BY RADIATION

Beside the heat loads caused by convection/conduction during the thermal quench, radiation could also lead to heat fluxes close to the PFC melting limits in ITER. During natural disruptions in JET, strong poloidal peaking of the heat fluxes by radiation have been reported, with peaking factor of up to 3.5 during VDE [26]. With MGI, the radiation is very localised in the early pre-TQ phase at the location the gas enters the plasma, but extends poloidally and toroidally in the later phase and generates a radiating mantle around the remaining core plasma just before the thermal quench (see figure 3). In the current quench, most of the radiation is found in the plasma center. The poloidal peaking factor of the heat flux at the wall caused by radiation is below 1.7 for most of the disruption phases (figure 14). A strong poloidal peaking of up to 2.5 is found in the pre-TQ phase. It has to be noted that the tomographic reconstruction of the radiation measured by bolometry is based on two cameras, which are $\Phi = 90^\circ$ and $\Phi = -135^\circ$ away from the injection port. Because the radiation spreads along the inclined field lines, it is expected that the radiation cloud is artificially broadened in poloidal direction, resulting in underestimated poloidal peaking factors.

In order to estimate the toroidal peaking, visible radiation recorded by a fast camera viewing the injection section has been analysed. An example of the visible emission in the range of about 400

– 700nm as recorded by the fast camera during neon injection is shown in figure 15. The emission along the green line has been taken to reconstruct toroidal profiles. Figure 16 shows such profiles for different times after valve opening (t_0) during neon injection at 1.7 MPa into L-mode plasma. Using simplifying assumptions, we can calculate an upper limit of the toroidal radiation peaking factor (TRPF). We assume that the total radiation consists only of visible emission, neglecting therefore the emission from ions with higher degree of ionisation, which have a broader distribution around the injection point. The bolometry, 90° toroidally separated from the injection port, measures a radiated energy during the pre-TQ phase equal to about 80 – 100% of the thermal energy loss. Radiation for $\phi > 90^\circ$ is assumed to be zero. In contrast to the analysis of the poloidal profiles, only peaking of the emission profiles is considered, not the peaking of the resulting heat flux on the PFC. Integration of the emission along the line of sight has not been corrected. Figure 17 shows the estimated toroidal peaking for L-mode and H-mode. During the initial phase, the peaking factor is very high, reducing to 5 – 8 in the later pre-TQ phase. The TRPF is slightly higher in H-mode compared to L-mode, but no dependence on the DMV pressure - beside the temporal behaviour - is found.

5. GENERATION AND MITIGATION OF RUNAWAY ELECTRONS

Runaway generation is observed with injection of pure neon and argon. Argon injection leads for all possible gas amounts and for magnetic fields above 1.8 T to runaway currents of up to 50% of the initial plasma current. Traces of runaways indicated by neutron radiation can be found for Ar MGI even at magnetic fields down to 1.2 T. Runaway generation during Neon injection is much weaker and occurs in most cases in the tail of the current quench phase. No runaway generation is observed during injection of the deuterium mixtures, pure deuterium and helium.

It is assumed that in present-day tokamaks the primary runaway electrons during disruptions are mainly generated by the Dreicer mechanism [27]. A second generation mechanism could be caused by the fast cooling during the thermal quench, and is referred to as hot tail generation [28]. In ITER additional sources of runaway electrons exists, which are independent from plasma density and electric field and can not be suppressed. The primary runaways are then multiplied by the avalanche process [29]. Suppression of the Dreicer mechanism happens at densities of the order of 10^{20} m^{-3} in JET, whereas the suppression of the avalanche requires total electron densities (free and bound electrons) above $n_e = 10^{21} \text{ m}^{-3} \times E/V\text{m}^{-1}$. In this respect, we are interested to inject a high number of electrons. Figure 18 is similar to figure 5b, with the difference that this time, the number of injected electrons $N_{e,CQ}$ is plotted. Although Ne or Ar have a high atomic number, their slow delivery through the long tube, causes less electrons being injected compared to He or D_2 . But not only the number of injected electrons is of interest, also the assimilation in the plasma has to be sufficiently high to achieve relevant densities. The impurity density in the current quench plasma $N_Z(CQ)$ can be estimated from the current decay time by using a simple model for the current decay, which includes plasma and vessel current as well as the power balance $\text{Prad} = P_{OH}$ (see section 8 and [11]). This model can be applied, if the radiation is predominantly caused by the injected species, which is expected for argon. In order to compare to the data shown in figure 9, the linear current quench times have

been calculated as function of the number of impurities in the plasma. These values were fitted to the measured τ_{CQ} (blue and black line in figure 9), resulting in an assimilation efficiency $N_Z(CQ)/N_{inj,CQ}$ of $50 \pm 10\%$ (Ar/D₂) and $65 \pm 35\%$ (Ar). With Ar injection we see a tendency towards higher assimilation efficiencies with decreasing q_{95} . The same trend can be seen for Ne, where a shorter τ_{CQ} is achieved for $q_{95} = 3.1$. Unfortunately, a quantitative analysis as for Ar is not possible for He, D₂ and Ne and their assimilation efficiencies remain unknown for these experiments. In order to investigate the dependency of the assimilation efficiency on plasma parameters further, a scan of the plasma current has been performed either with constant B_t or with constant q_{95} . The data shown in figure 19 shows a clear increase of the efficiency with lower q_{95} , whereas no influence by the plasma current is observed if B_t is adjusted such to keep q_{95} constant. This dependence on q_{95} is consistent with what has been seen at DIII-D from direct density measurements [8].

The fraction of critical density achieved with Ar/D₂ and pure Ar injection is given in figure 20a as function of the injected amount of gas prior to the current quench and in 20b for the plasma current scan. The electric field has been calculated from the maximum current decay $E = L_p dI_p/dt(\max)/2\pi r$ with inductance $L_p = 1.2\mu_0 R_0 l_i/2$ considering only the magnetic energy stored inside the vessel. Since the vessel resistive time is about 4 ms, this is justified for the early phase of the current quench. As in [2], the inductance has been corrected to take into account the flattening of the current profile during the thermal quench. The electric field ranges from 18Vm^{-1} to 28Vm^{-1} for Ar/D₂ and from 23Vm^{-1} to 42Vm^{-1} for pure Ar (both cases with $I_p = 2.0\text{MA}$). A clear increase with the number of impurities injected can be seen. However, with the present set-up, MGI at JET reaches only up to 4% of the critical density at $I_p = 2.0\text{MA}$. Because the electric field increases with plasma current, a reduction in n_e^{tot}/n_c is seen with increasing I_p and constant q_{95} . Also the reduced assimilation efficiency at higher q_{95} is reflected in the data shown in figure 20. NBI heated pulses show a slightly higher n_e^{tot}/n_c .

6. DISCUSSION

In this section, we briefly discuss two import issues for ITER, the radiation load at the injection port and the suppression of the runaway avalanche.

6.1. HEAT LOADS FROM LOCAL RADIATION

Beryllium melting by local radiation at the injection port during the pre-TQ phase is of concern for ITER and could be the boundary condition determining the minimum number of injection ports necessary. The local heating of PFCs in the vicinity of the injection port in JET can be estimated from the peaking factors TRPF ≈ 5.0 and PRPF ≈ 2.0 , the energy loss in the pre-TQ phase of $\Delta W_{\text{pre-TQ}} \approx 2 \text{ MJ}$ and the duration of the pre-TQ phase of $\Delta t_{\text{pre-TQ}} \approx 5\text{ms}$. The maximum heat load parameter from these numbers for JET is $2\text{MJm}^{-2}\text{s}^{-0.5}$ translating into a temperature rise of about 150 K. Unfortunately, this estimated temperature rise cannot be confirmed by IR camera measurements as they are disturbed during the gas injection by radiation from the plasma itself. The present estimate for ITER for the pre-TQ phase is a loss of thermal energy of $W_{\text{pre-TQ}} = 180\text{MJ}$ by

radiation within 7ms [4]. With toroidal and poloidal peaking factors of 5-8 and 2.0, respectively, we find a heat load parameter of $40 - 64 \text{ MJ s}^{-0.5} \text{ m}^{-2}$ for a single injection point. The Be melting limit of about $15 \text{ MJ s}^{-0.5} \text{ m}^{-2}$ suggests the use of at least 3-4 injection ports in ITER. A more precise analysis would require modelling of the toroidal spread of the radiation or direct measurements of toroidal profiles of the total radiation.

6.2. SUPPRESSION OF THE RUNAWAY AVALANCHE

Suppression of the runaway avalanche requires significant higher densities than presently achieved in JET. As a consequence more gas has to be supplied on a shorter time scale. In order to illustrate the challenging requirements for such a gas injection system, we extrapolate from existing data using equation 1. The cooling duration $\Delta t_{\text{pre-TQ}}$ is given in figure 21 as function of the pressure in the DMV. These calculations show that a further increase of the pressure will indeed increase $N_{\text{inj,CQ}}$, but is technically limited. Further increase can only be achieved by enlarging the valve orifice and/or a shortening of the distance between valve and plasma. An example with orifice diameter of 10cm and only 1m distance to plasma is given in figure 21, showing that with this already demanding set-up an increase of $N_{\text{inj,CQ}}$ by a factor 10 could be feasible, still not enough to reach the critical density in JET. However, this simplified estimate is done on the basis that the relation $P_{\text{rad}} \sim N_Z$ can be extrapolated to these amounts of gas, resulting in an extremely short pre-TQ phase in the sub-millisecond range. This might be a pessimistic assumption, because plasma parameters like the finite initial electron density might cause a saturation in the radiated power. It might as well be too optimistic, because it assumes that the assimilation efficiency does not degrade with the number of injected particles.

Experiments with higher $N_{\text{inj,CQ}}$ are urgently needed to draw a conclusion for ITER. But it becomes already obvious from the above calculations that the valve exit in ITER has to be close (of the order of a 1 m) to the plasma edge. Because of the neutron and gamma radiation loads, such a set-up is extremely challenging. JET data shows that the current decay rate with argon injection is already at the eddy current limit for ITER. A further increase in the injected amount of gas could imply further acceleration of the current quench and therefore lead to unacceptable forces. It remains an open question, if effects like opacity could prevent further acceleration of the current quench. If this is not the case, neon or deuterium mixtures might be the only candidates to avoid a too fast current quench.

SUMMARY AND CONCLUSIONS

The experiments with massive gas injection at JET have shown that this concept is able to significantly reduce the loads during disruptions. Halo currents are reduced by up to a factor of 4, sideways forces even by more than a factor of 10 during VDE. The heat loads during the thermal quench can be reduced by the enhanced radiation. The fraction of radiated energy varies between 50% and almost 100%, depending on the analysis method. This uncertainty could be overcome by a full energy balance done either by including heat fluxes to the divertor and main chamber or by

calculations of the magnetic energy dissipated in the surrounding structures. Runaway generation is successfully avoided by injecting mixtures of Ne or Ar with 90% deuterium. However, only a maximum of about 5% of the critical density for the suppression of the runaway avalanche is achieved.

The optimum gas to be used for active disruption mitigation in JET with the present valve set-up is Ar mixed with 90% D₂. This gas mixture provides a short time of flight of about 2 ms combined with a short cooling phase of about 5 ms with prepressure of 3.5 MPa and therefore a total reaction time of only 7ms which is compatible even with fast VDEs. The fast current decay allows for efficient reduction of halo currents and sideways forces. This gas mixture also prevents from runaway generation and radiates a high fraction of the thermal energy. We have not discussed the impact of MGI on wall deconditioning and impurity contamination in the subsequent pulse. Work presented in [16] shows that mixtures with deuterium lead to wall loading with deuterium, resulting in a non-sustained breakdown for the pulse following the injection. There is also indication of an increased impurity concentration in the subsequent pulse and conditioning procedures might be necessary to reduce the impurity contamination. Therefore, it is necessary to have an advanced disruption detection scheme in JET to decide whether MGI is to be activated in a developing disruption or the disruption loads can be tolerated and mitigation is not needed.

ACKNOWLEDGEMENTS

This work was supported by EURATOM and carried out within the framework of the European Fusion Development Agreement. The views and opinions expressed herein do not necessarily reflect those of the European Commission.

APPENDIX - CURRENT QUENCH MODEL

Impurity densities can be estimated from the current decay rate using a simple model. This model consists of equations for the plasma and vessel current I_p , I_v , treating both as lumped wires:

$$\frac{dI_p}{dt} = \frac{2\pi R\eta I_p}{A_p (L_p/L_v)} = \frac{I_v}{\tau_v d(1-L_p/L_p)} , \quad (3)$$

$$\frac{dI_v}{dt} = \frac{dI_v}{\tau_v} = \frac{dI_p}{dt} , \quad (4)$$

with plasma cross section area I_p , plasma and vessel inductance L_p , L_v , plasma resistivity η and vessel L/R time τ_v . A_p and L_p are assumed constant during the part of the current quench considered here. The current quench plasma temperature is defined by assuming that the ohmic power is compensated completely by radiation:

$$n_e n_Z L_Z(T_e) = \frac{\eta(T_e) I_p^2}{A_p^2} , \quad (5)$$

with impurity density n_Z and impurity emissivity L_Z . The latter is taken from data derived from corona equilibrium [30].

The above equations are used to fit the current evolution in the range 100% to 50% of I_p at the start of the current quench. An example is given in figure 22 with $L_p = 3.9\mu\text{H}$, $L_v = 0.7\mu\text{H}$, $A_p = 4.5\text{m}^2$, $\tau_v = 2.1\text{ms}$. The experimental data deviates from the model for lower currents. This could be attributed to a change in A_p and L_p because of vertical displacement of the plasma column and related shrinking of the plasma cross section.

REFERENCES

- [1]. G.F. Matthews et al., Physica Scripta **T138** (2009) 014030
- [2]. M. Lehnen et al., Journal Nuclear Materials **390-391** (2009) 740.
- [3]. G. Arnoux et al., 19th PSI conference 2010.
- [4]. M. Sugihara, IEA Workshop on Key ITER Disruption Issues, Culham, October 2009.
- [5]. N. Commaux et al., Nuclear Fusion **50** (2010) 112001.
- [6]. D.G. Whyte et al Journal Nuclear Materials **363-365** (2007) 1160-7.
- [7]. G. Pautasso et al., Plasma Phys. Control. Fusion **51** (2009) 124056.
- [8]. E.M. Hollmann et al., Nuclear Fusion **48** (2008) 115007.
- [9]. M. Bakhtiari et al., Nuclear Fusion **45** (2005) 318325.
- [10]. A.J. Thornton et al., Journal Nuclear Materials (2011) in press, doi:10.1016/j.jnucmat.2010.10.029
- [11]. S.A. Bozhenkov et al., Plasma Physics and Controlled Fusion **50** (2008) 105007.
- [12]. C. Reux et al., Nuclear Fusion **50** (2010) 095006.
- [13]. U. Kruezi et al., 36th EPS Conference on Plasma Phys. Sofia, June 29 - July 3, ECA 33E, P-2.153 (2009).
- [14] M. Lehnen et al., 36th EPS Conference on Plasma Phys. Sofia, June 29 - July 3, ECA 33E, O-2.001 (2009).
- [15]. S.A. Bozhenkov et al, JET Experiments on Massive Gas Injection, 51st APS Meeting, Atlanta, 2009
- [16]. U. Kruezi et al., 19th PSI conference, San Diego (2010).
- [17]. S.A. Bozhenkov et al., 36th EPS Conference on Plasma Physics Sofia, June 29 - July 3, ECA 33E, P-1.180 (2009)
- [18]. K.H. Finken et al., Nuclear Fusion. **51** (2011) 033007.
- [19]. S.A. Bozhenkov et al., to be published in Nuclear Fusion (2010).
- [20]. V. Riccardo et al., Plasma Physics and Controlled Fusion **47** (2005) 117.
- [21]. M. Sugihara et al., Nuclear Fusion **47** (2007) 337.
- [22]. Hender T.C. et al 2007 Progress in the ITER Physics Basis, Chapter 3: MHD stability, operational limits and disruptions, Nuclear Fusion **47** (2007) S128.
- [23]. S.N. Gerasimov et al., Scaling JET disruption sideways forces to ITER, EPS 2010 Dublin, P4.121.
- [24]. T.C. Hender et al., this conference, EXS/10-3.

- [25]. J.I. Paley et al., *Journal Nuclear Materials* **337-339** (2005) 702.
 [26]. A. Huber et al., 19th PSI conference, San Diego (2010).
 [27]. J. W. Connor and R. J. Hastie, *Nuclear Fusion* **15** (1975) 415.
 [28]. H. Smith et al., *Phys. Plasmas* **12** (2005) 122505.
 [29]. M. N. Rosenbluth and S. V. Putvinski, *Nuclear Fusion* **37** (1997) 1355.
 [30]. H.P.Summers "The ADAS User Manual" (2004), version 2.6; <http://adas.phys.strath.ac.uk>

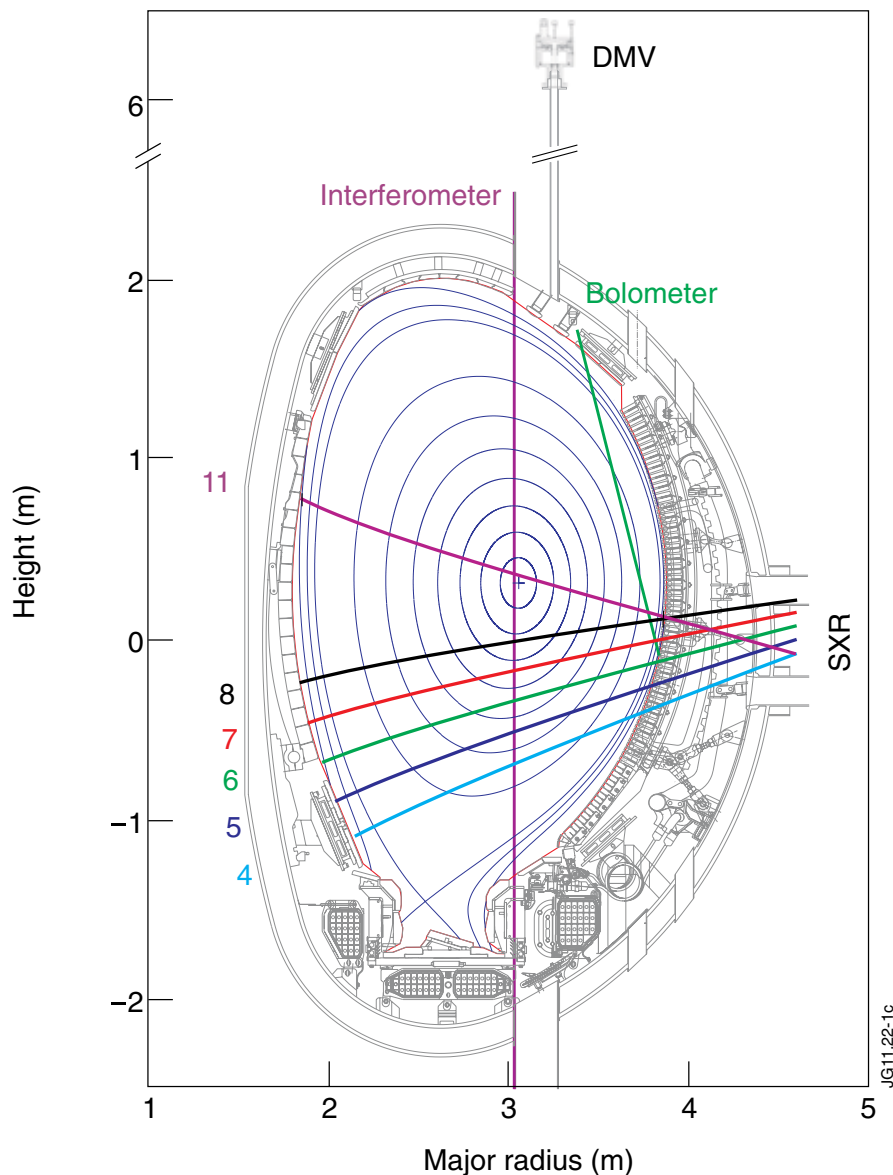


Figure 1: Set-up of the disruption mitigation valve at JET. The valve is situated at the end of a 4 m tube with 40 mm diameter. Equilibrium reconstruction for NBI heated pulse (Pulse No: 77808). The lines of sight used for the estimate of the time of flight are given in green for bolometry and in magenta for interferometry. The SXR channels are used in section 2 to document the penetration of the cooling front.

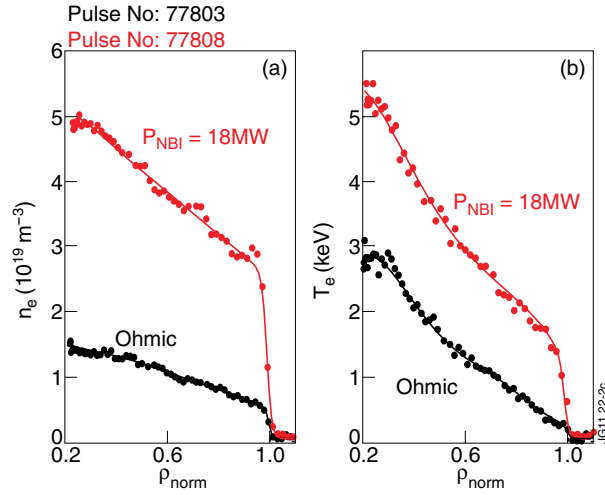


Figure 2: Electron density (a) and temperature (b) profiles for ohmic heating only and for $P_{\text{NBI}} = 18 \text{ MW}$ (averaged over 0.5s, $I_p = 2.0 \text{ MA}$, $B_T = 3.0 \text{ T}$).

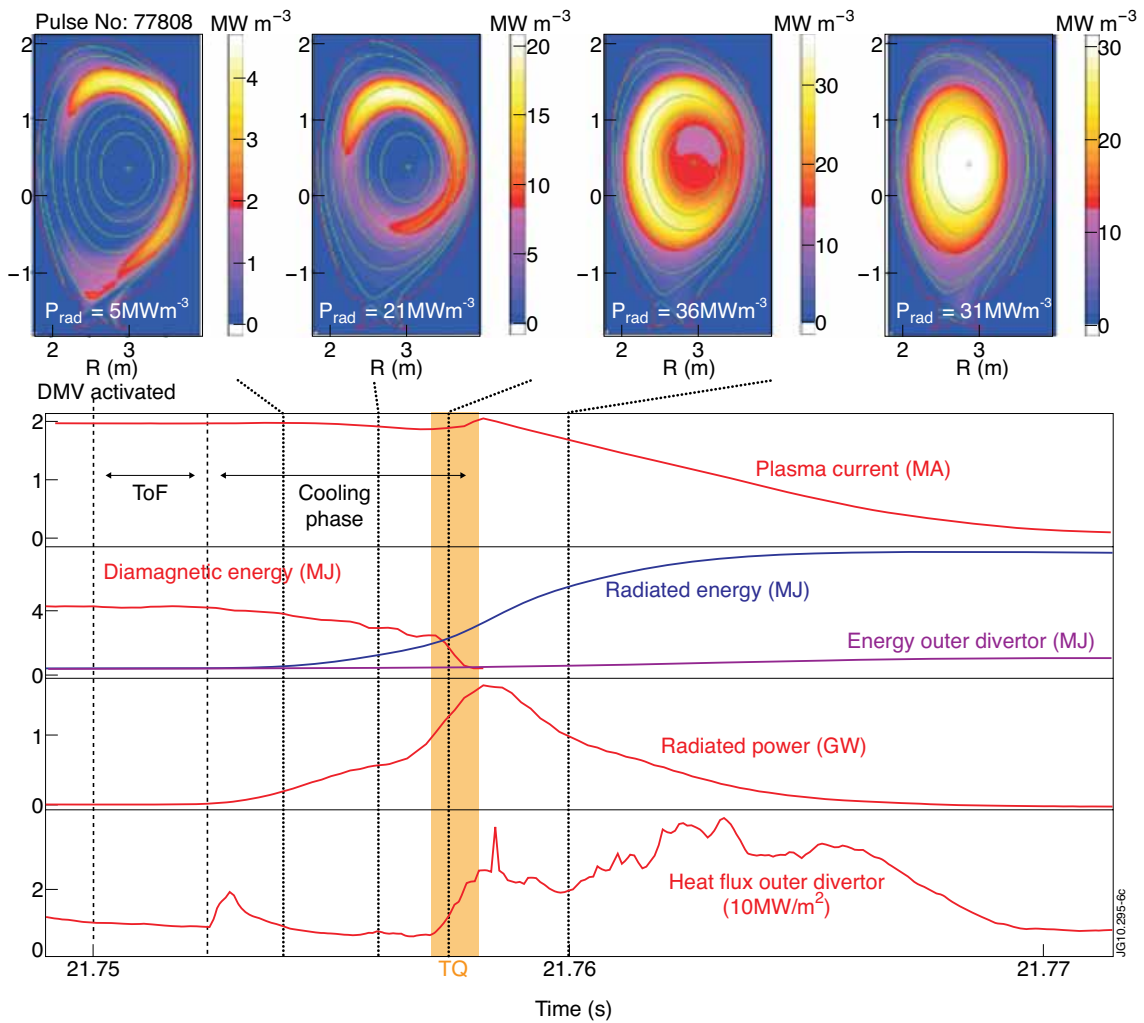


Figure 3: Disruption sequence. Ar/D_2 injection, $P_{\text{DMV}} = 3.6 \text{ MPa}$.

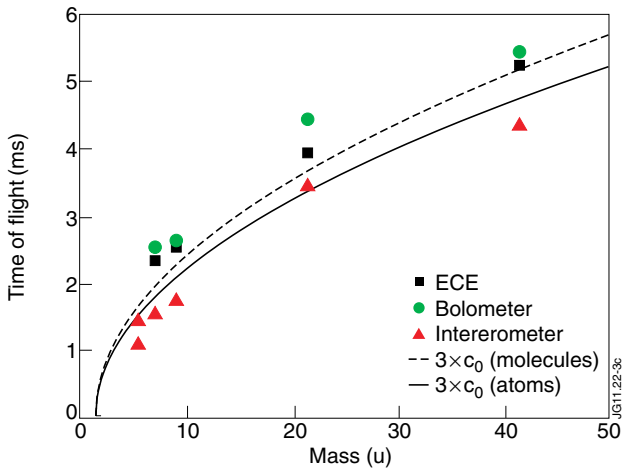


Figure 4: Time of flight estimated from measurements of ECE, bolometer and interferometer.

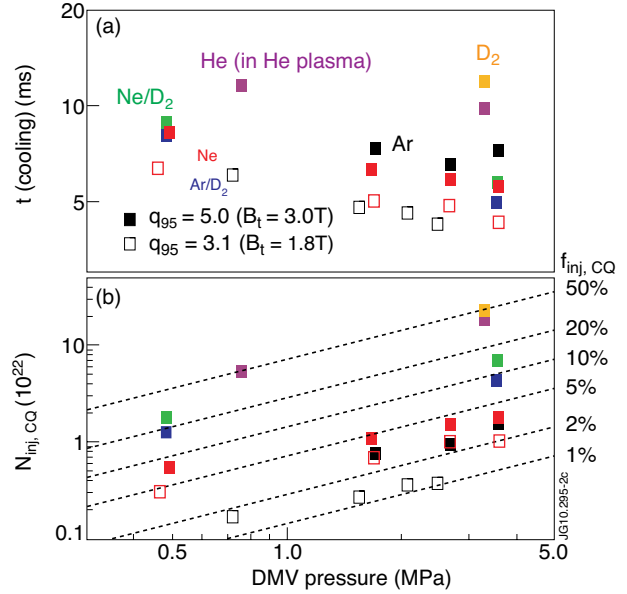


Figure 5: Duration of the cooling phase (a) and calculated number of injected particles before the current quench (b) (ohmic plasmas).

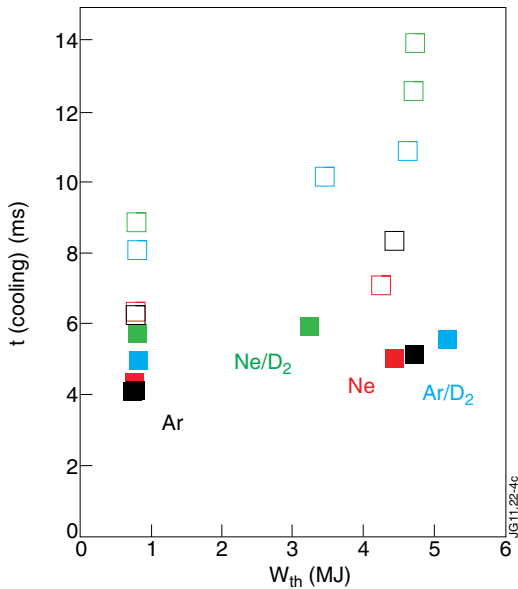


Figure 6. Duration of the cooling phase as function of stored thermal energy for $P_{DMV} > 3MPa$ (closed symbols) and $P_{DMV} < 1MPa$ (open symbols). Data for D_2 mixtures is for $q_{95} = 5.0$ and data for pure gases is for $q_{95} = 3.0$.

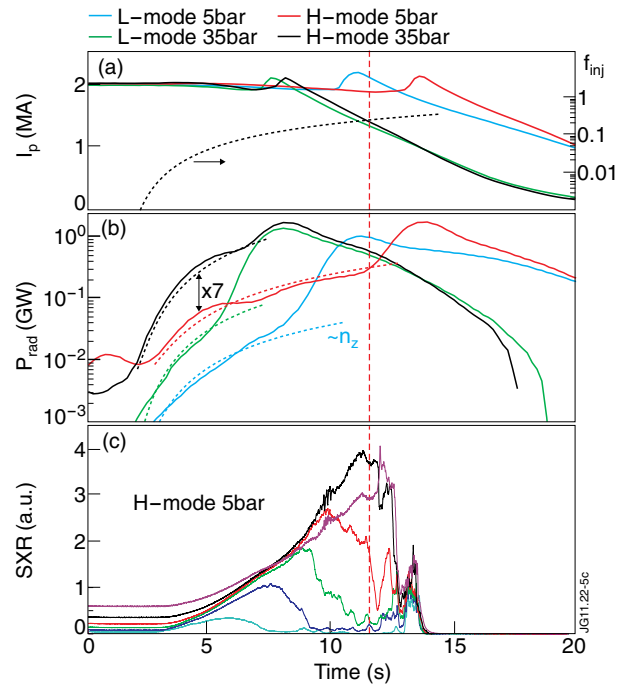


Figure 7. Plasma current (a) and radiation (b) during MGI for Ar/ D_2 injection (Pulse No's: 76803/4,76807/8). The dashed line in (a) gives the fraction of injected gas. The DMV is activated at $t = 0$. SXR data for the H-mode disruption at 0.5MPa is given in (c). See figure 1 for colour coding.

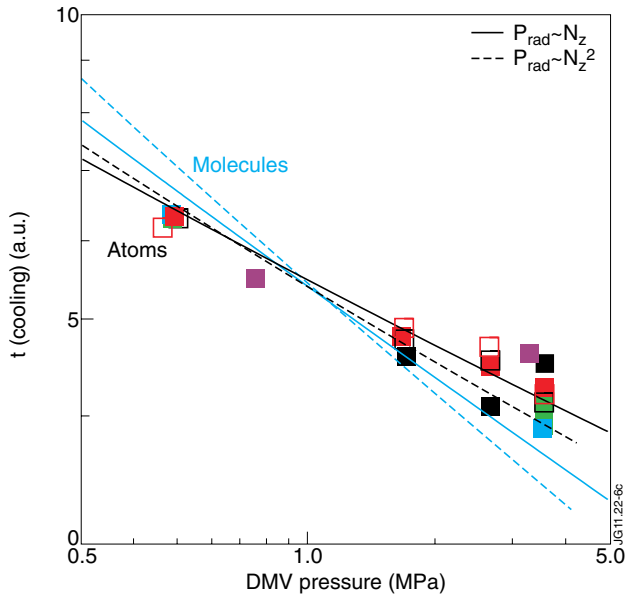


Figure 8: Cooling time scaled for comparison. Lines give the cooling time according to equation 1. Color code as in figure 5.

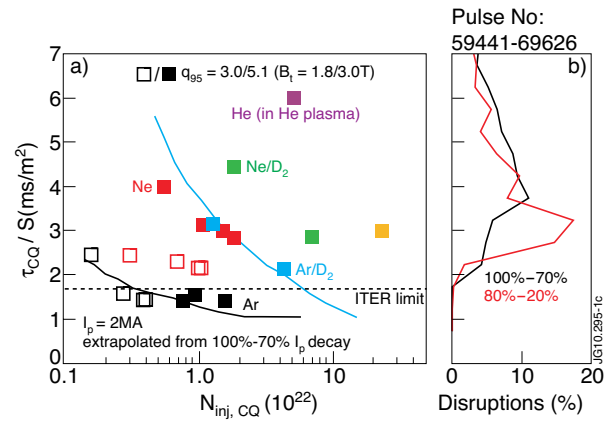


Figure 9: Linear current decay time for MGI (a) and reference database (b). Solid lines in (a) are from estimated impurity densities (see section 5).

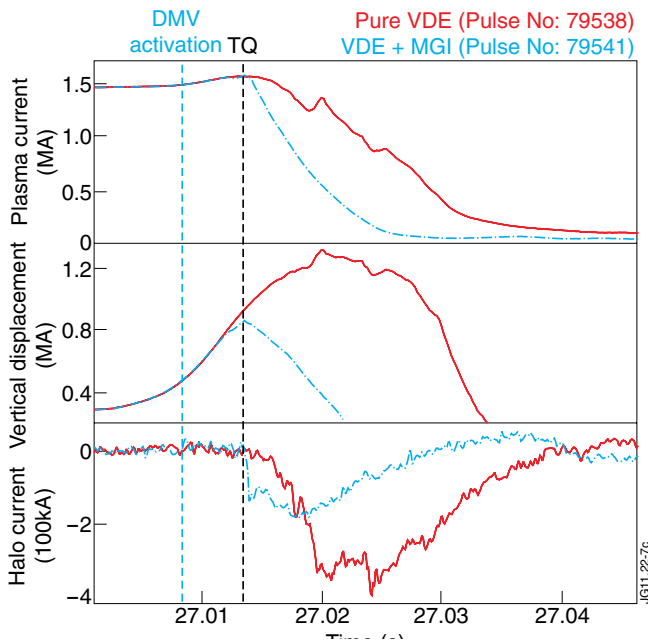


Figure 10: Evolution of deliberate VDEs: red curves are from a pure VDE and blue curves from MGI into a developing VDE where the current quench was initiated about 7ms after $t(\Delta z = 10\text{cm})$.

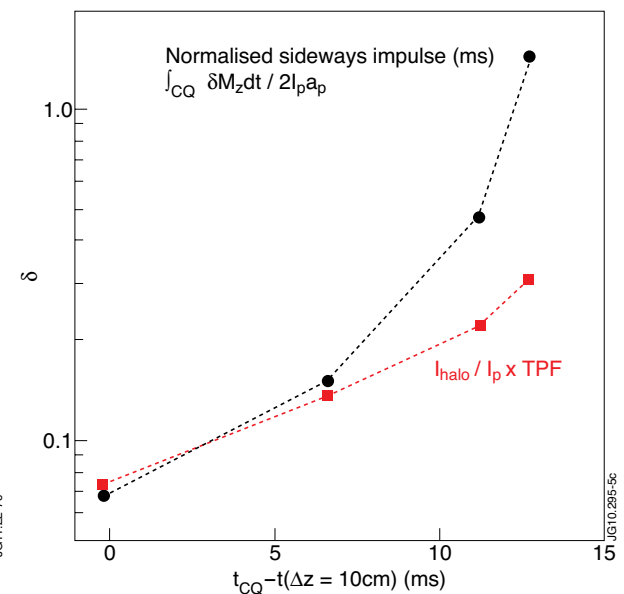


Figure 11: Reduction of halo currents and sideways forces.

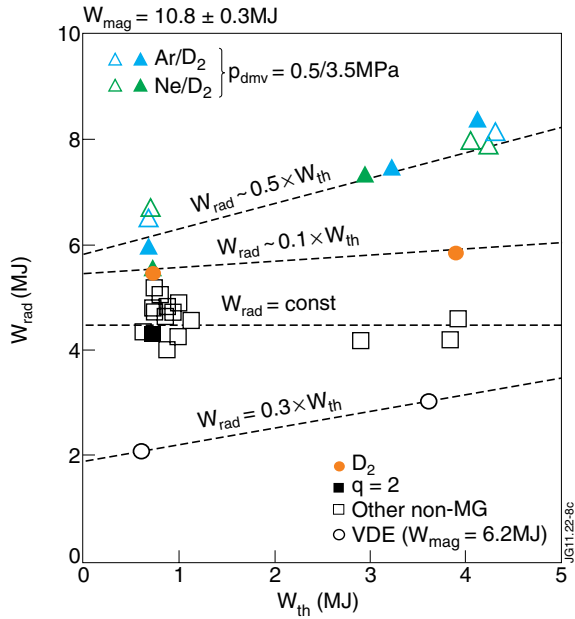


Figure 12: Energy radiated during the entire disruption (including pre-TQ, TQ and CQ phase) as function of initial stored thermal energy.

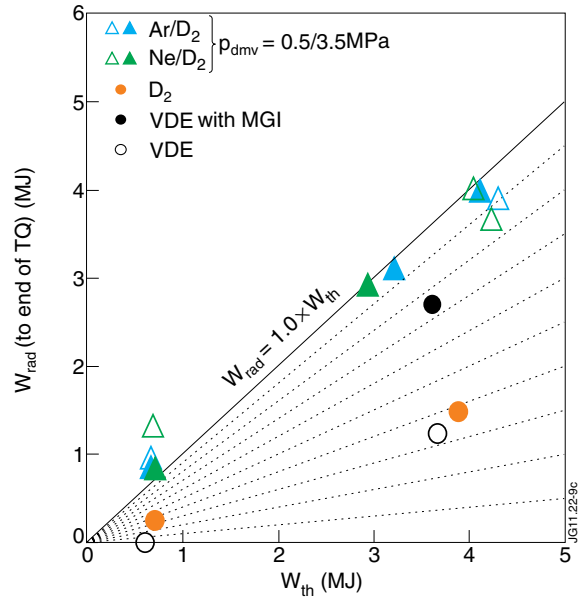


Figure 13: Energy radiated until the end of the thermal quench as function of initial stored thermal energy.

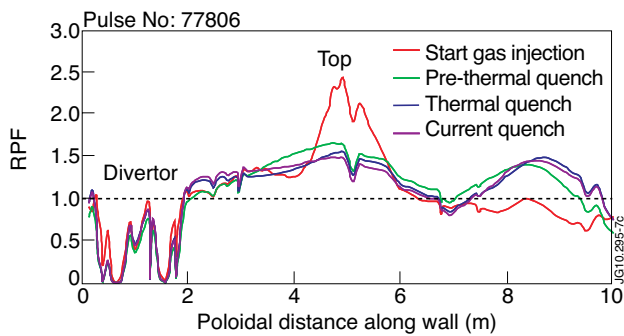


Figure 14: Poloidal radiation peaking factor (PRPF) during Ar/D₂ injection into H-mode plasma [26].



Figure 15: Fast camera image overlaid on an image of the vessel taken during the H-mode phase ($t - t_0 = 6.9\text{ms}$).

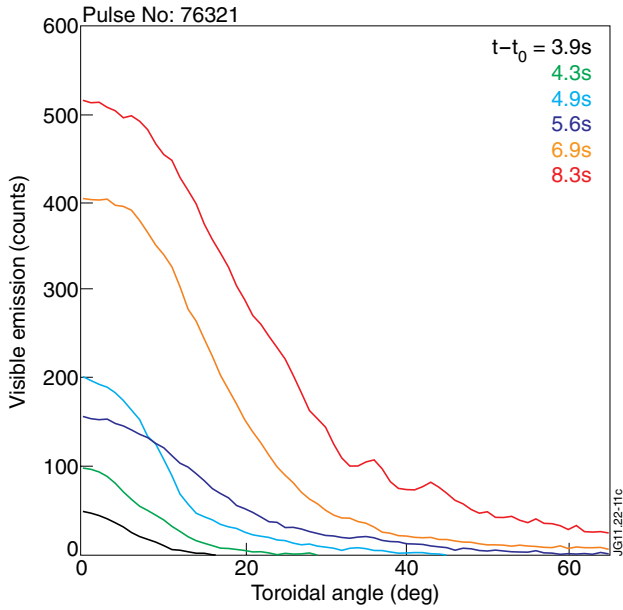


Figure 16: Toroidal profiles of the visible emission at the injection port.

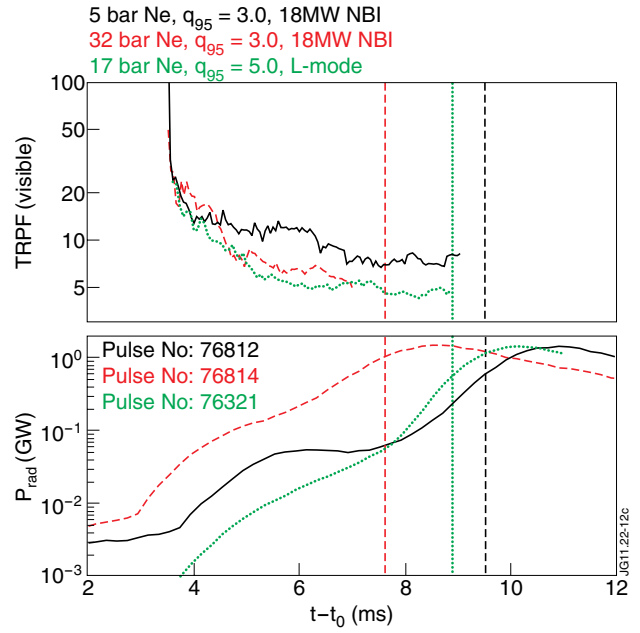


Figure 17: Toroidal Radiation Peaking Factor (TRPF) estimated from profiles of the visible emission during the cooling phase and radiated power measured at $\Phi = 90^\circ$. Vertical lines indicate TQ .

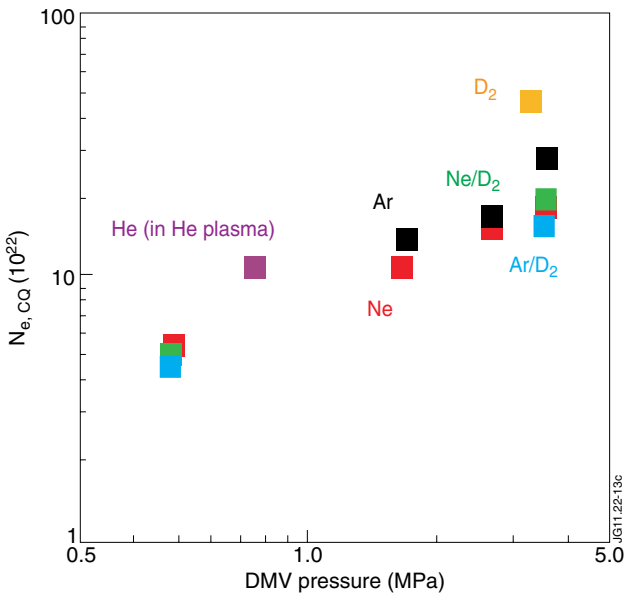


Figure 18. Number of electrons injected before the current quench (L-mode, $q_{95} = 5.0$).

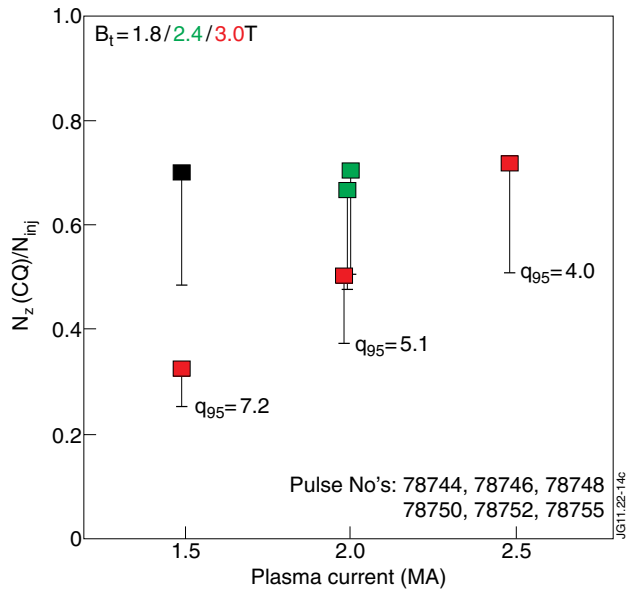


Figure 19: Assimilation efficiency at the start of the thermal quench as indicated by SXR. The errorbar indicates the efficiency at the end of the thermal quench by assuming an average TQ duration of 1 ms. The impurity density has been calculated by fitting the current from 100% to 50% of $I_p(t = 0)$. Ar/ D_2 injection at 3.2MPa, 18MW NBI.

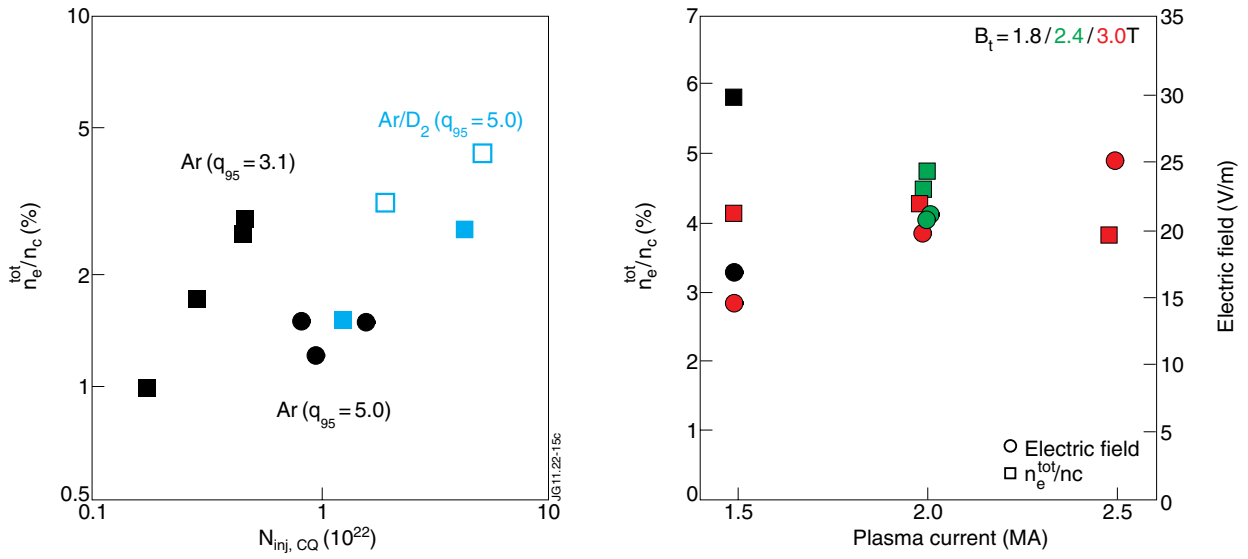


Figure 20: Total electron density normalised to the critical density for unconditional suppression of runaway electrons, which has been calculated from the maximum electric field during the CQ; a) for different DMV pressure (closed symbols - ohmic heating only, open symbols - 18MW NBI), b) for the I_p/q_{95} scan discussed in figure 19 (18MW NBI).

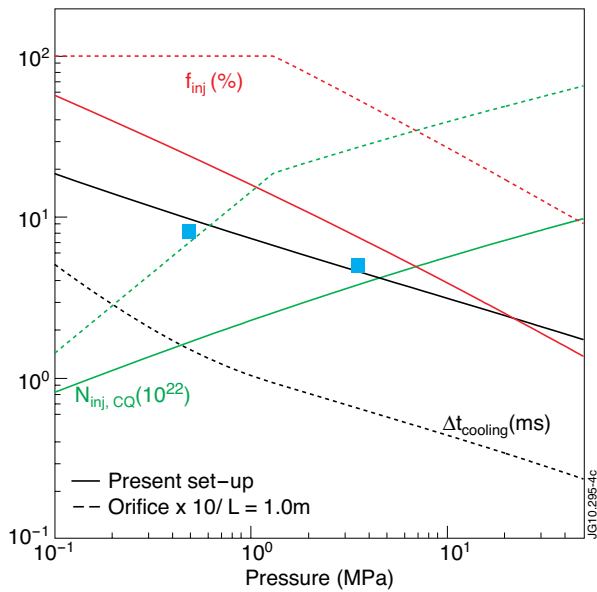


Figure 21: Extrapolation of gas injection towards runaway suppression. Blue squares mark the measured $\Delta t_{cooling}$ for Ar/D₂.

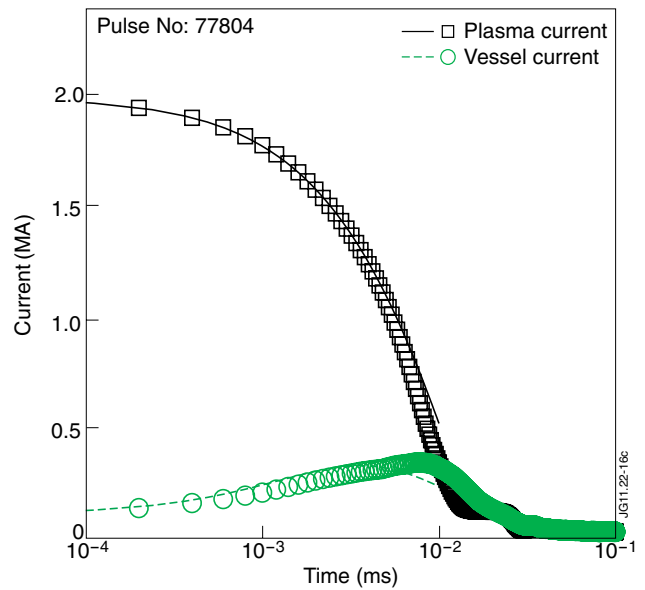


Figure 22: Current decay (symbols = experiment, lines = model). The data fit results in $T_e(t=0) = 3.5\text{eV}$, $n_z = 3.7 \times 10^{20} \text{ m}^{-3}$.